

Electrochemically induced hyperfluorescence based on the formation of charge-transfer excimers

Chang-Ki Moon^{1,2}, Yuka Yasuda³, Yu Kusakabe³, Anna Popczyk¹, Shohei Fukushima³, Julian F. Butscher¹, Hironori Kaji^{3*}, Malte C. Gather^{1,2*}

¹Humboldt Centre for Nano- and Biophotonics, Institute for Light and Matter, Department of Chemistry and Biochemistry, University of Cologne, Greinstr. 4-6, 50939 Köln, Germany

²Organic Semiconductor Centre, SUPA, School of Physics and Astronomy, University of St Andrews, North Haugh, St Andrews KY16 9SS, United Kingdom

³Institute for Chemical Research, Kyoto University, Uji, Kyoto, Japan

Keywords: Electrochemiluminescence, hyperfluorescence, electrochemically induced hyperfluorescence, charge-transfer excimer, energy transfer, spectroelectrochemistry

Despite the extensive use of electrochemiluminescence in sensing applications, its potential in lighting and display technology has been constrained by the low luminance and short operational lifetime of electrochemiluminescence devices (ECLDs). Here, we demonstrate a substantial enhancement in the luminance, efficiency, and operational longevity of ECLDs by introducing electrochemically induced hyperfluorescence (ECiHF) via electrogeneration of charge-transfer (CT) excimers and subsequent energy transfer to fluorescent acceptors. By assuming a double-decker arrangement of the electron donor and acceptor groups, the molecule TpAT-tFFO supports solution-state thermally activated delayed fluorescence from a CT excimer state and efficient energy transfer to the rubrene dye TBRb. Optimized ECLDs based on this material combination achieve an unprecedented luminance of 6,220 cd/m² and their operational lifetime (LT₅₀) at an initial luminance of 100 cd/m² exceeds 20 minutes, more than 10-fold longer than other ECLDs with meaningful efficiency or brightness. We identify energy level alignment between the excimer and the emitter as a crucial factor for efficient ECiHF. In mixtures with energy gaps > 0.5 eV, electron transfer results in reduced performance and renders the operation strongly dependent on applied voltage and frequency. By contrast, spectroelectrochemical analysis reveals that devices with favorable energy level alignment operate on a pure excimer mechanism across a wide range of frequencies. These findings highlight the innovative potential of ECiHF in improving the performance of ECLD, which can be widely applied in future commercial lighting solutions.

By combining electrochemistry with light emission, electrochemiluminescence (ECL) has become a versatile tool in biomedical research, particularly for sensitive detection of biomolecules in immunoassays and diagnostics¹⁻³, food safety analysis⁴, and environmental surveillance⁵. To extend the ECL technology to lighting and display applications, and hence to further benefit from its cost-effectiveness and scalability, recent research has explored novel luminophores, electrode configurations, and operation mechanisms to enhance the brightness, efficiency, and operational stability of electrochemiluminescent devices (ECLDs)⁶⁻¹³.

Achieving intense ECL necessitates production of abundant radical ions and their subsequent rapid radiative recombination. However, any accumulation of radical ions can trigger side reactions that deteriorate the luminophores in the device¹⁴, limiting the maximum brightness of ECLDs that rely on annihilation processes to less than 700 cd/m² and restricting their operational times to only a few minutes. To overcome this limitation, we recently suggested an operational mechanism based on exciplex formation by mixing heterogeneous electron-donating and accepting materials with a rubrene dye in a solution^{15,16}. This approach partially mitigated the accumulation of rubrene radical ions, improving the stability and peak luminance compared to ECLDs based on the previously used annihilation process.

In organic light-emitting diodes, luminophores supporting thermally activated delayed fluorescence (TADF) have gained great popularity as they raise the proportion of emissive singlet excitons to ~100% by rapidly depopulating non-emissive triplet states via reverse intersystem crossing (RISC) processes^{17,18}. In ECLDs, TADF emitters have been demonstrated to achieve up to a 4-fold improvement in ECL efficiency¹⁹⁻²¹; however, so far with limited benefit to the maximum achievable luminance and operational stability. Using TADF emitters in ECLDs also presents additional challenges, particularly related to solvent selection, as positive solvatochromism leads to significant spectral shifts and broadening of the emission in high-polarity solvents^{22,23}. As an alternative, hyperfluorescence (HF), combining a

conventional fluorescent emitter with a triplet sensitizer²⁴, offers the potential for high luminance and efficiency without suffering from substantial spectral shifts. In our previous exciplex-based ECLDs^{15,16}, the exciplex state served as a triplet sensitizer^{25,26}, but the RISC process on the exciplex was not sufficiently rapid to support HF. Using HF promises to further enhance the brightness and stability of ECLDs, even though identifying donor-acceptor pairs with sufficient RISC rate, solubility and a suitably staggered band alignment remains challenging.

In this paper, we realize electrochemically induced hyperfluorescence (ECiHF) through the electrogeneration of charge-transfer (CT) excimers—rather than CT exciplexes—, thus achieving rapid RISC and subsequent energy transfer to a fluorescent emitter. Our approach uses two TADF molecules, the recently reported TpAT-tFFO²⁷ and the unpublished TpATtBu-tFFO, which feature face-to-face alignment of the donor and acceptor components, thus exhibiting excellent TADF characteristics. Using concentration-dependent photoluminescence (PL) spectroscopy in solution, we observe a transition from monomer emission to excimer emission while preserving clear hallmarks of TADF as the concentration of TpAT-tFFO increases. Adding a rubrene dye to these high-concentration TpAT-tFFO solutions then leads to the appearance of HF and enables ECiHF in AC-operated ECLDs facilitating record-high luminance, efficiency, and operational stability. In addition, we investigate the excimer of TpATtBu-tFFO which has higher energy than that of the TpAT-tFFO excimer but in ECLDs shows lower performance with a stronger dependence on operating voltage and frequency. Absorption spectroelectrochemistry confirms excimer formation as the primary operating mechanism in TpAT-tFFO devices. At the same time, it reveals a mixed operation mechanism for TpATtBu-tFFO devices, where excimer formation and ionic annihilation compete. A schematic illustration of the ECiHF mechanism is given in Fig. 1a. By alternately applying positive and negative voltages to the electrodes, oxidized and reduced products of the monomer

accumulate near each electrode surface. Redox products recombine to form electrostatically bound CT excimers, with the highest occupied molecular orbital (HOMO) and lowest unoccupied molecular orbital (LUMO) localized on donor and acceptor segments of TADF molecules, respectively, resulting in minimal orbital overlap and thus in efficient intermolecular CT transition. The CT excimers undergo intersystem crossing (ISC) and RISC cycles, and transfer singlet energy to neighboring fluorescent emitters through FRET, which eventually leads to a higher than 25% exciton utilization.

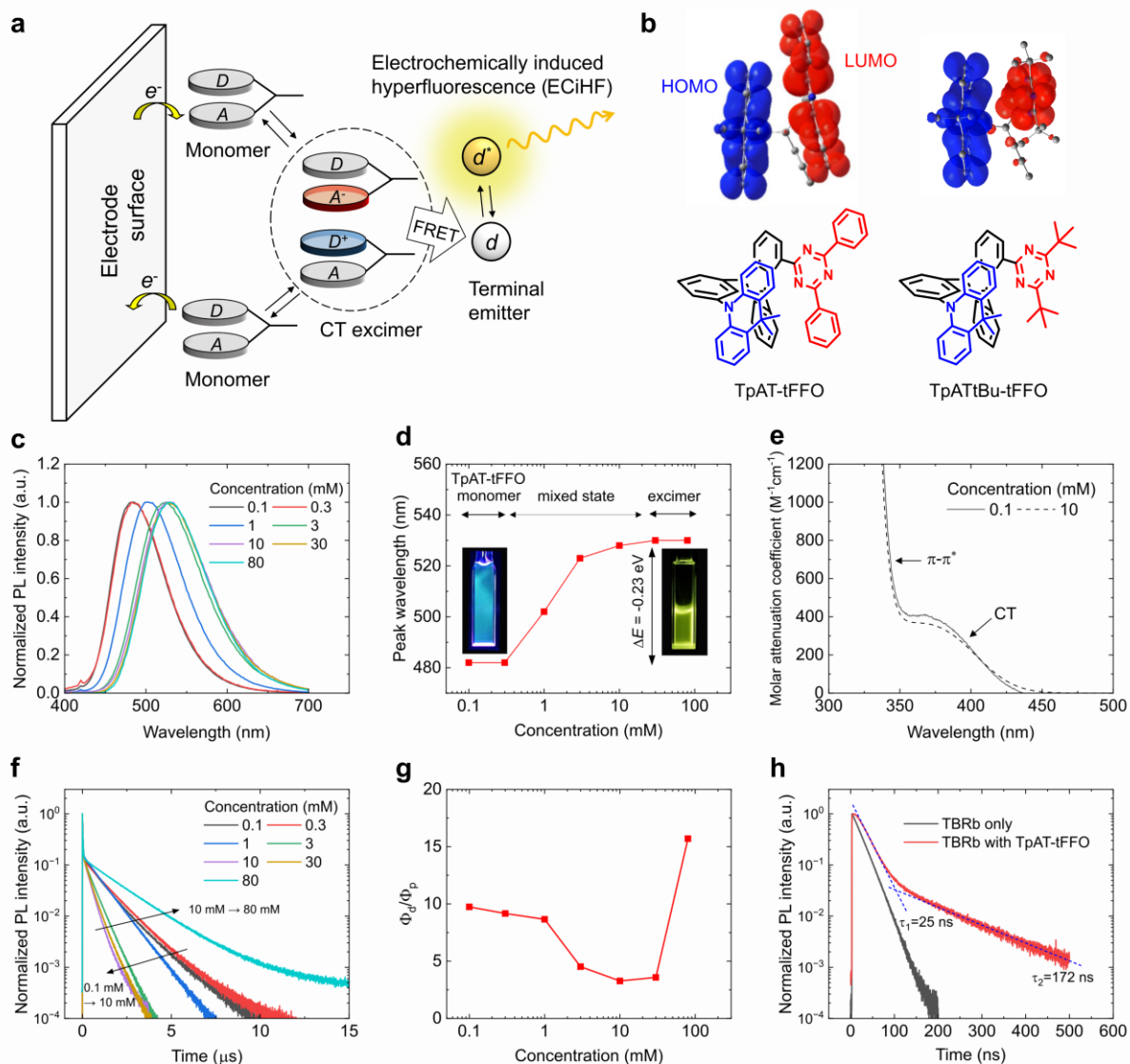


Fig. 1. Electrochemically induced hyperfluorescence (ECiHF). **a**, A schematic of ECiHF under AC operation with formation of CT excimers and energy transfer to the terminal emitter. **b**, Molecular structures of TpAT-tFFO and TpATtBu-tFFO in three-dimensional configurations, with the donor and acceptor groups represented as blue and red segments, respectively, in line drawings. For both molecules, the HOMO (blue surface) and LUMO (red surface) states are separated on the donor and acceptor groups, respectively. **c**, Photoluminescence (PL) spectra of TpAT-tFFO in a 2:1 by volume mixture of toluene and acetonitrile. **d**, Peak PL wavelength of PL for TpAT-tFFO at concentrations ranging from 0.1 mM to 80 mM. **e**, Molar attenuation of TpAT-tFFO measured at concentrations of 0.1 mM and 10 mM. **f**, Transient PL of TpAT-tFFO at concentrations ranging from 0.1 mM to 80 mM. **g**, Ratio of the quantum yield of delayed to prompt fluorescence (Φ_d/Φ_p) against TpAT-tFFO concentration. **h**, Transient PL of solution containing 10 mM of TBRb and 80 mM of TpAT-tFFO, compared to solution containing 10 mM of TBRb only.

Fig. 1b shows three-dimensional representations of the molecular structures of TpAT-tFFO and TpATtBu-tFFO. The triptycene linkers in these compounds enable a face-to-face alignment of the donor (dimethyl dihydrouridine) and acceptor groups (either diphenyl triazine or di-ter-butyl triazine), with the HOMO and LUMO localizing on the donor and acceptor groups, respectively. The “double-decker” structures are further expected to facilitate intermolecular π - π stacking at high concentrations. Consequently, these molecules are expected to allow intramolecular²⁷ as well as intermolecular CT transitions.

The concentration-dependent PL spectra of TpAT-tFFO solutions in a 2:1 by volume mixture of toluene and acetonitrile showed a shift in emission from blue fluorescence (482 nm) at <0.3 mM to green fluorescence (530 nm) at >30 mM (Figs. 1c and 1d). The gradual red-shift indicates the transition from monomer to excimer emission, with the saturation in spectral shift at 30 mM indicating that pure excimer state is reached at this concentration. According to our previous TD-DFT calculations for TpAT-tFFO²⁷, the energy level of the singlet CT state increases as the donor-acceptor separation increases. A reduction in energy by 0.23 eV corresponds to a decrease in separation from 4.72 Å (intramolecular CT state) to 4.00 Å (intermolecular CT state), driven by strong intermolecular electrostatic binding. Unlike for the emission, the absorption spectra (spectrally resolved molar extinction coefficient) of TpAT-tFFO at concentrations of 0.1 mM and 10 mM are largely identical, with no red-shift of the CT absorption observed with increasing concentration (Fig. 1e). This indicates negligible intermolecular interactions of TpAT-tFFO in the ground state, even though strong intermolecular binding occurs upon excitation. Transient PL measurements indicate TADF is present observed across all concentrations tested here (Fig. 1f). The ratio of the photoluminescence quantum yield (PLQY) of the delayed and prompt emission (Φ_d/Φ_p) was higher for the excimer emission at high concentrations than for the monomer emission, while the ISC-RISC processes showed comparable rates (see Fig. 1g and Supplementary Table 1).

Adding 10 mM 2,8-di-tert-butyl-5,11-bis(4-tert-butylphenyl)-6,12-diphenyltetracene (TBRb) to an 80 mM excimer solution of TpAT-tFFO yielded pure HF, with prompt and delayed fluorescence lifetimes of 25 ns and 172 ns, respectively (Fig. 1h) and no sign of residual excimer emission in this mixture (see Supplementary Fig. 1). The HF is facilitated by the very fast RISC on the excimer (rate constant of $8.2 \times 10^7 \text{ s}^{-1}$) and also by rapid FRET.

Adding a supporting electrolyte to the hyperfluorescent solution, we fabricated two types of ECLDs with sandwich-electrode configurations (Fig. 2a). The first, a glass-glass device, uses two ITO-coated glass substrates, separated by a 30-micrometer gap filled with the solution and had four square-shaped emissive surfaces measuring 4 mm^2 each (see Methods for detailed fabrication process). The intensity of light emitted through both substrates was equal due to the optically symmetric structure of the device; luminance values quoted in the following refer to the light emission to one side only. The second configuration, a glass-mirror device, includes a silver mirror with a passivation coating on the outer side of one of the glass substrates to reflect the emission back into and through the device and thus achieve unidirectional and therefore brighter emission through one of the substrates.

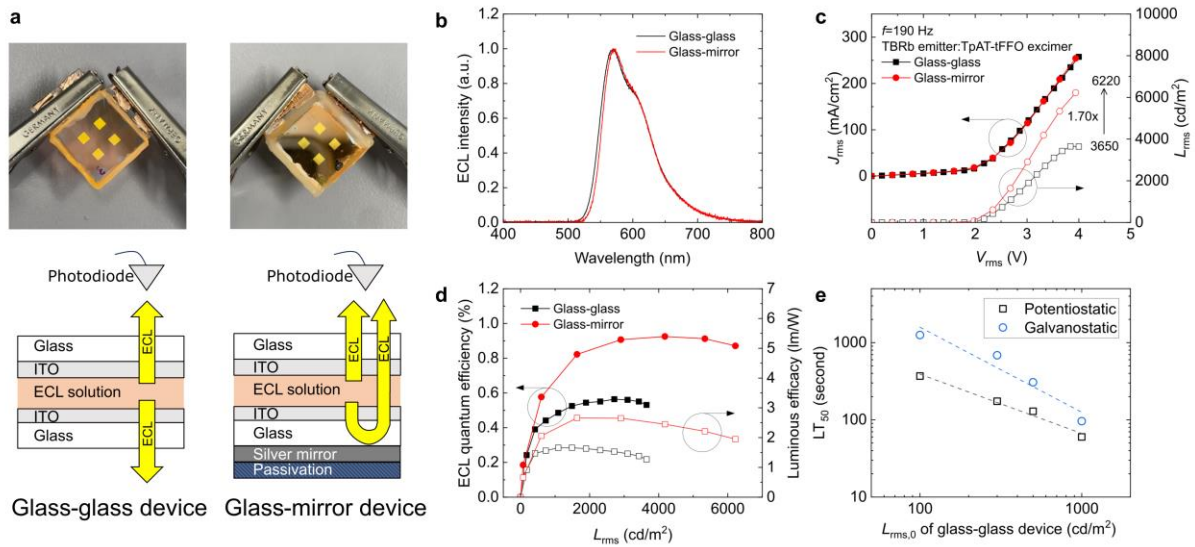


Fig. 2. ECLDs operating based on the ECiHF mechanism using TpAT-tFFO as excimer-forming material and TBRb as terminal emitter. a, Photographs and structures of glass-glass and glass-mirror device configurations with 4 pixels, each measuring 2 mm by 2 mm, operated simultaneously. **b,** ECL spectrum of each device. **c,** Root-mean-square (rms) current-voltage-luminescence (JVL) characteristics. **d,** Quantum efficiency and luminous efficacy. Data obtained under AC operation at a frequency of 190 Hz. **e,** Operational lifetime LT_{50} of the glass-glass device under potentiostatic and galvanostatic operation, respectively. All data based on emissions through one substrate side only.

Fig. 2b shows the ECL spectra of these two devices; these peaks both at 570 nm, clearly indicated light emission is exclusively from TBRb. The glass-mirror devices showed a slightly reduced emission intensity at wavelengths shorter than the peak wavelength due to self-absorption by TBRb during light recycling. Fig. 2c shows the root-mean-square (rms) current density-voltage-luminescence (JVL) characteristics of both devices under AC operation at a frequency of 190 Hz. Both devices showed very similar current-voltage characteristics due to their identical electrochemical nature. The glass-glass device achieved a luminance of 3,650 cd/m² at $V_{rms}=4.0$ V, while the glass-mirror device showed a 1.70-fold enhancement, reaching a maximum luminance of 6,220 cd/m². The ECL quantum efficiency (Φ_{ECL}) and luminous efficacy (LE) shown reached maximum values of 0.56% and 1.66 lm/W, respectively, for the glass-glass device (only considering the emission in one direction), and 0.93% and 2.66 lm/W for the glass-mirror device (Fig. 2d). The glass-mirror device thus showed an improvement in

luminance, LE, and Φ_{ECL} , by 1.60 to 1.70-fold. This enhancement, unfortunately, was less than the theoretical improvement of 1.97 expected when only considering the reflectivity of an ideal silver surface. This loss is likely due to differences in the ITO surface condition between the two devices as the UV-ozone treatment of ITO had to be reduced from the optimum duration of 15 minutes to 3 minutes post-coating of the silver mirror, which in turn will affect the faradaic process during device operation. Self-absorption by TBRb might further contribute to the lower-than-expected brightness in the glass-mirror device.

Fig. 2e shows estimates of LT_{50} of our glass-glass ECLDs, obtained by measuring the time until the ECL intensity decreases to 50% of the maximum value when continuously operated under AC driving (see luminance vs time curves in Supplementary Fig. 2). Under potentiostatic (voltage-controlled) operation, the LT_{50} values were 369 and 60 seconds at initial luminance levels of 100 cd/m^2 and 1000 cd/m^2 , respectively. Under galvanostatic (current-controlled) operation, the LT_{50} values for these initial luminance levels improved to 1252 and 96 seconds, respectively.

Table 1 summarizes the performance of the ECLDs in this study and compares them to prior works using the same sandwich-electrode configurations but different operation mechanisms, i.e. exciplex formation and ionic annihilation. Devices based on excimer formation outperformed annihilation-based devices in luminance as they use a more efficient bimolecular recombination process. The excimer-based device achieved a further improvement in luminance, Φ_{ECL} , and operational lifetime over the exciplex-based device. We attribute this improvement to two factors: (1) the presence of ECiHF with rapid ISC/RISC cycles the CT excimer, and (2) the excimer's greater robustness against chemical degradation at high-voltage and during prolonged operation. The glass-mirror device achieved an unprecedented ECL luminance of 6,220 cd/m^2 by reflection of back-emission. Galvanostatic operation enhanced the LT_{50} lifetime relative to potentiostatic operation, due to the better charge carrier regulation

which maintains ionic balance¹³, and reduces local thermal stress due to local concentrations in charge flux at protruded regions of the slightly rough ITO surface²⁸. As a result, the CT excimer-based device achieved an LT_{50} value exceeding 1,200 seconds at an initial luminance of 100 cd/m^2 , to our best knowledge, surpassing the current record of 1,000 seconds for a much dimmer ECLD using a $\text{Ru}(\text{bpy})_3^{2+}$ luminophore with TiO_2 nanoparticles (peak luminance is only 165 cd/m^2)²⁹.

Table 1. Summary of characteristics of ECLDs with sandwich-electrode configurations and different operation mechanisms using AC driving. *M* indicates a device with a mirror coating on one substrate side. *T* indicates a device with a mesoporous TiO_2 electrode. *P* and *G* represent potentiostatic voltage-controlled and galvanostatic current-controlled operation during lifetime measurements, respectively. Reference ¹⁶ reported Φ_{ECL} values of 0.35% and 0.52% for operation at 300 Hz and 100 Hz, respectively; this table shows the Φ_{ECL} value at 300 Hz, at which the device showed higher luminance. Reference ¹³ measured the lifetimes at an initial luminance of approximately 115 cd/m^2 and demonstrated a further improvement in lifetime for a floating-electrode configuration. Reference ²⁹ measured the lifetime at an initial luminance of 165 cd/m^2 .

Operational mechanism	Material	Medium	L_{max} (cd/m^2)	LE_{max} (lm/W)	Φ_{ECL} (%)	LT_{50} (sec), $L_0 \sim 100 \text{ cd/m}^2$
CT excimer (this work)	TBRb & TpAT-tFFO	toluene-acetonitrile	3650, 6220 (<i>M</i>)	1.66, 2.66 (<i>M</i>)	0.56, 0.93 (<i>M</i>)	1252 (<i>G</i>), 369 (<i>P</i>)
Exciplex ^{15,16}	TBRb, TAPC & TPBi	toluene-acetonitrile	1250, 2260 (<i>T</i>)	1.17, 2.06 (<i>T</i>)	0.38	75 (<i>P</i>)
Annihilation ¹⁵	TBRb	toluene-acetonitrile	390	0.74	-	26 (<i>P</i>)
Annihilation _{13,30}	$\text{Ru}(\text{bpy})_3^{2+}$	ionic liquid	700	0.20	-	300 (<i>G</i>), 50 (<i>P</i>)
Annihilation ²⁹	$\text{Ru}(\text{bpy})_3^{2+}$ & TiO_2 nanoparticles	propylene carbonate	165	-	-	1000 (<i>P</i>)

The second excimer-forming material, TpATtBu-tFFO, has a higher band gap (3.25 eV) than TpAT-tFFO (2.86 eV). It exhibited an analogous monomer-to-excimer transition with increasing concentration as TpAT-tFFO, shifting from deep-blue monomer emission at 442 nm to greenish-blue excimer emission at 484 nm (Fig. 3a). The excimer emission also exhibited

strong delayed fluorescence, with a higher Φ_d/Φ_p than the monomer emission (see Supplementary Table 2 and Supplementary Fig. 3). The emission of the TpATtBu-tFFO excimer showed a stronger overlap with TBRb absorption than the TpAT-tFFO excimer (see Supplementary Fig. 4), thus potentially offering better ECiHF performance with even more efficient FRET in a device using TpATtBu-tFFO than the devices using TpAT-tFFO (referred to in the following as TpATtBu-tFFO device and TpAT-tFFO device, respectively).

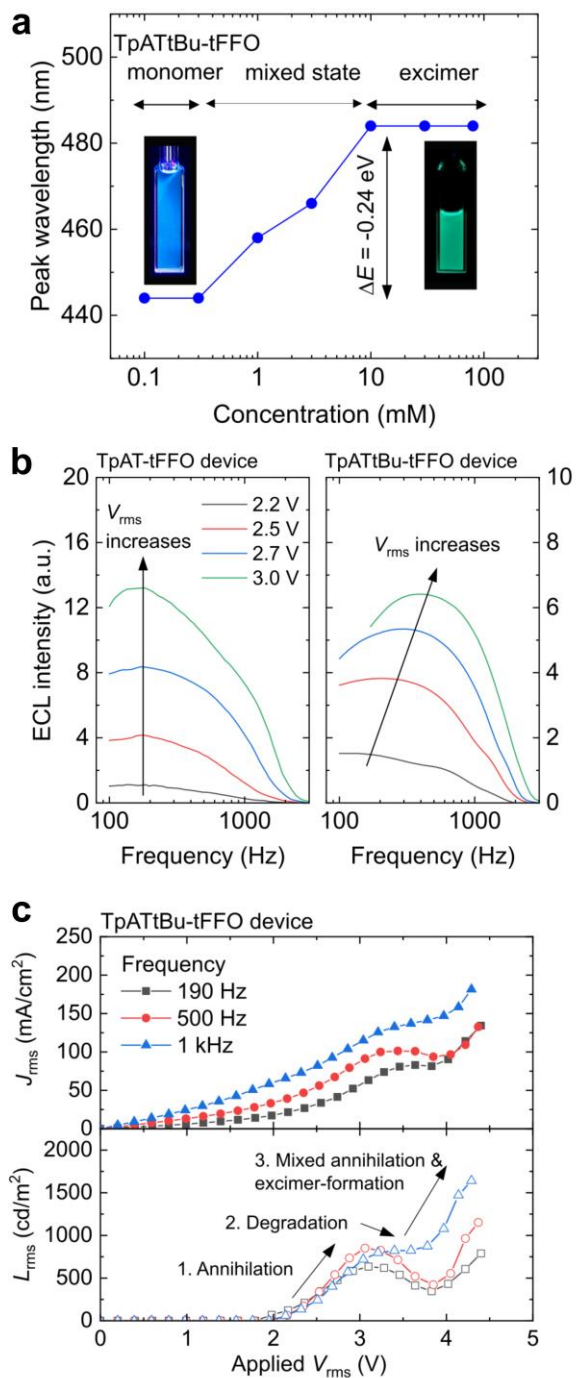


Fig. 3. ECLDs based on excimer formation in TpATtBu-tFFO. **a**, Shift in PL emission peak with concentration of TpATtBu-tFFO, demonstrating the transition from monomer to excimer emission. **b**, Frequency-dependent ECL intensity at different applied voltages, comparing TpAT-tFFO and TpATtBu-tFFO devices. **c**, Rms J/L characteristics of the TpATtBu-tFFO device operating at 190 Hz, 500 Hz, and 1 kHz.

Fig. 3b compares the frequency-dependent ECL intensity of TpAT-tFFO and TpATtBu-tFFO devices (glass-glass) at different applied voltages. While no shift in optimal frequency ($f = 190$

Hz) was observed in the TpAT-tFFO device, a gradual upward shift was noted in the TpATtBu-tFFO device. Additionally, the TpATtBu-tFFO device showed S-shaped JV characteristics, i.e. a simultaneous decrease in current density and luminance at $V_{\text{rms}} > 3.0$ V, followed by an increase in both as the voltage continued to rise to even higher values (Fig. 3c). A similar S-shaped JV curve was observed in an ECLD based on annihilation between TBRb ions¹⁵, when rapid degradation of TBRb molecules occurred. However, in contrast to the TBRb devices, our TpATtBu-tFFO device displayed a subsequent increase in luminance at higher voltage. These observations suggest that the TpATtBu-tFFO device operates through a mixed mechanism of ionic annihilation and excimer-formation. Below $V_{\text{rms}} = 3.0$ V, the annihilation dominates, leading to rapid degradation of TBRb molecules. As the voltage increases beyond this threshold, the excimer-formation process begins to be effective, increasing the luminance as this process does not involve TBRb ions. Despite this, both processes still occur simultaneously, with their relative contributions varying depending on the operation frequency. Higher frequencies resulted in increased luminance, with a maximum of 1,640 cd/m² achieved at $f = 1$ kHz.

To gain deeper insights into the differences between TpAT-tFFO and TpATtBu-tFFO devices, the spectroelectrochemical analysis illustrated in Fig. 4a was performed³¹. This technique tracks changes in optical density (ΔOD) when light passes through the active area of the ECLD with and without an applied voltage. A positive ΔOD indicates the presence of electrogenerated ionic species, and a negative ΔOD represents the loss of neutral species due to faradaic processes. Since our analysis uses a one-second acquisition time, much longer than a single AC cycle, it is particularly sensitive to the accumulation of ions involved in slower reaction pathways. In contrast, ions undergoing rapid processes are less detectable as they revert to neutral states quickly during acquisition.

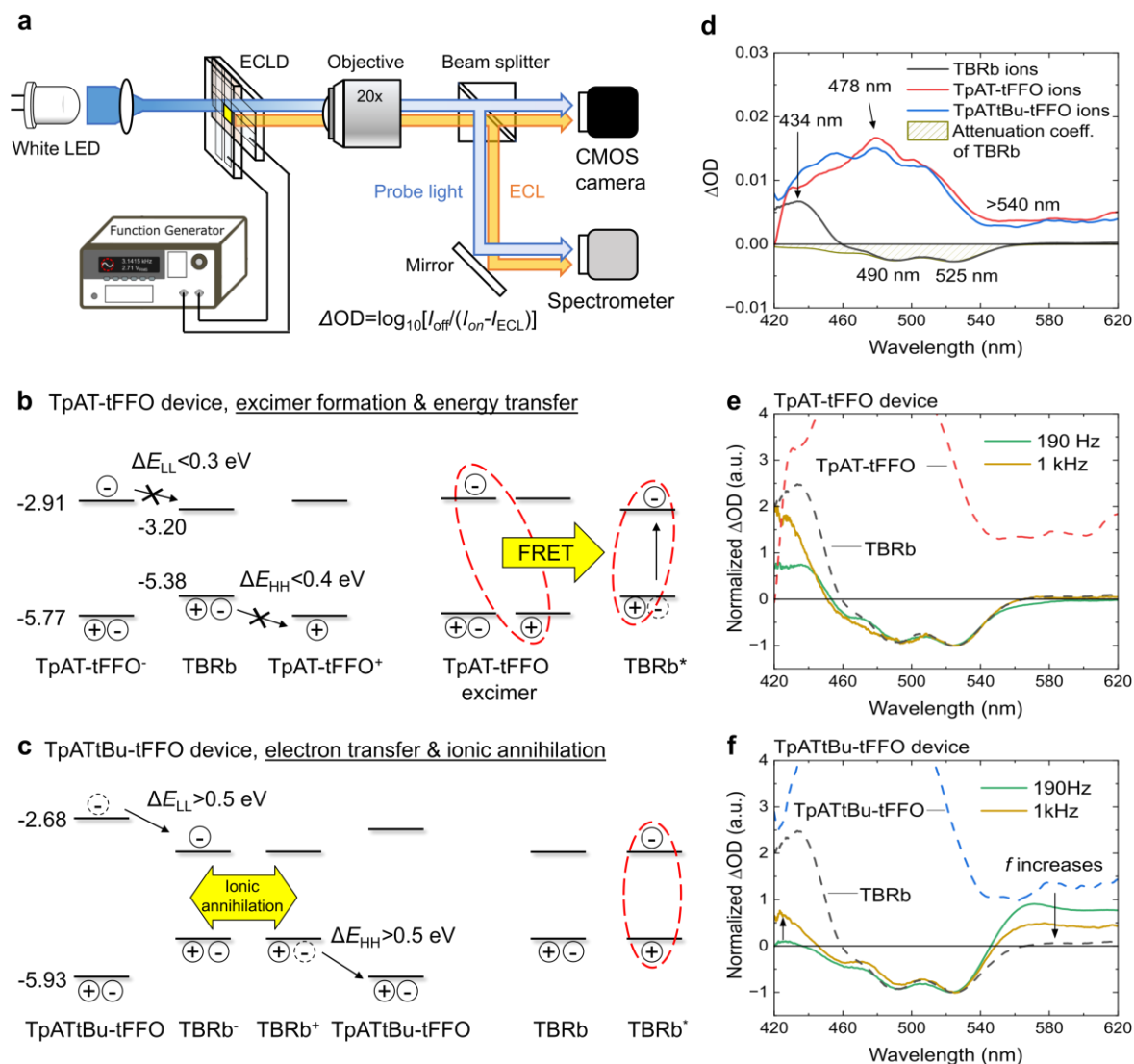


Fig. 4. Absorption spectroelectrochemistry. **a**, Schematic of the measurement setup. **b**, Schematics of the ECL processes based on the excimer-formation on TpAT-tFFO and subsequent energy-transfer to TBRb. ΔE_{HH} and ΔE_{LL} represent the gaps between the HOMO and LUMO levels, respectively. **c**, Schematic of electron-transfer between TpATtBu-tFFO and TBRb and subsequent ionic annihilation on TBRb. **d**, Measured absorption of TBRb, TpAT-tFFO, TpATtBu-tFFO ions under DC operation of each device. **e-f**, Spectroscopic analysis of change in optical density in TpAT-tFFO and TpATtBu-tFFO devices operated at frequencies of 190 Hz and 1 kHz. Changes are relative to the off-state of each device (see details in Methods).

Under an applied voltage two reaction pathways can produce a TBRb exciton. First, a cation and an anion of the monomers produced during the AC cycles can bind as a CT excimer, which

subsequently transfers energy to a TBRb molecule (Fig. 4b). Second, the ions of these monomers can transfer electrons to two separate TBRb molecules, creating a TBRb cation and anion, which subsequently annihilate to produce a TBRb exciton (Fig. 4c). The gaps in HOMO and LUMO levels (ΔE_{HH} and ΔE_{LL} , respectively) between TpATtBu-tFFO and TBRb are both larger than the corresponding gaps between TpAT-tFFO and TBRb, which may promote the second reaction pathway in the TpATtBu-tFFO system.

To test this hypothesis, first, we measured the absorption of TpAT-tFFO and TpATtBu-tFFO ions by applying a 3.5 V DC voltage to each device (Fig. 4d), which allowed for abundant ion production with minimal ionic annihilation/recombination. The absorption of TBRb ions was also measured using a device with a solution containing 10 mM TBRb with a supporting electrolyte. The TBRb ions showed an absorption peak at 434 nm, while the negative ΔOD peaks at 490 nm and 525 nm correspond to the loss of neutral TBRb molecules. TpAT-tFFO and TpATtBu-tFFO ions showed similar absorption spectra due to their structural similarities, with prominent peaks at 478 nm and a broad absorption band beyond 540 nm.

We then analyzed ΔOD under AC operation at $V_{rms} = 3.5$ V and at operating frequencies of 190 Hz and 1 kHz. For the TpAT-tFFO device (Fig. 4e), absorption by TBRb ions was detected near $\lambda = 434$ nm, but little absorption of TpAT-tFFO ions was observed at either frequency. This indicates that TpAT-tFFO ions are rapidly consumed via excimer formation, while TBRb ions possibly produced by direct ionization at the electrode surfaces accumulate. Consequently, these results, together with Figs. 2c and 3b, confirm that the TpAT-tFFO device operates through a robust CT excimer mechanism, unaffected by the applied voltage and operating frequency.

In contrast, for the TpATtBu-tFFO device (Fig. 4f), we simultaneously observed absorption by TBRb ions and the broad absorption band of TpATtBu-tFFO ions ($\lambda > 540$ nm). The absence

of TpATtBu-tFFO ion absorption at $\lambda = 478$ nm is likely because ions disappear rapidly through faradaic processes. Notably, as the frequency increased, the absorption of TpATtBu-tFFO ions reduced in magnitude, while the absorption signature of TBRb ions increased, indicating that the excimer-formation process accelerated. These findings confirm that while the TpATtBu-tFFO device operates through a mixed mechanism involving both excimer formation and ionic annihilation, the excimer formation process is more dominant at higher frequencies, in agreement with the upward shift of optimal frequency with increasing voltage (Fig. 3b) and the enhanced luminance at higher-frequency operation (Fig. 3c).

Taken together, these observations indicate that since ΔE_{HH} and ΔE_{LL} are both less than 0.40 eV relative to TBRb for TpAT-tFFO, fast excimer formation outcompetes electron transfer processes in the mixture. By contrast, for TpATtBu-tFFO, ΔE_{HH} and ΔE_{LL} both exceed 0.50 eV which promotes electron transfer processes that generate TBRb ions, particularly under a low-frequency AC operation.

In summary, we explored the mechanism of ECiHF and demonstrated significant improvements in luminance, efficiency, and brightness of ECLDs, enhancing their potential for future applications in lighting and display technologies. The TADF materials TpAT-tFFO and TpATtBu-tFFO formed CT excimers exhibiting strong delayed fluorescence characteristics at concentrations above 30 mM. Rapid RISC on the TpAT-tFFO excimer and subsequent FRET to fluorescent TBRb resulted in HF. An ECLD fabricated with two ITO-coated glass substrates achieved the maximum luminance of 3,650 cd/m² to one direction, while the luminance was further enhanced up to 6,220 cd/m² by a silver mirror coating to retro-reflect emission to the back side of the device. Additionally, from an initial luminance of 100 cd/m², the LT₅₀ values exceeded 6 minutes under potentiostatic operation and 20 minutes under galvanostatic operation, demonstrating the most stable ECLD operation reported to date.

We investigated the impact of energy level alignment between the excimer-forming materials and terminal emitter, finding that ΔE_{HH} and ΔE_{LL} of less than 0.4 eV is beneficial for efficient ECiHF. The device using TpAT-tFFO, where both gaps are below 0.4 eV, exhibited a monotonic increase in JVL , an optimal operating frequency (190 Hz) that was independent of applied voltage, and a robust excimer-formation process unaffected by operating frequency. By contrast, the device using TpATtBu-tFFO, where ΔE_{HH} and ΔE_{LL} are larger than 0.5 eV, showed S-shaped JVL curves relying on the frequency and an upward shift in the optimal frequency with increasing voltage, both of which likely originate from a mixed operational mechanism involving excimer formation and ionic annihilation. The spectroelectrochemical analysis indicated that at higher frequencies the predominant operation mechanism in the TpATtBu-tFFO device is excimer formation and subsequent energy transfer, whereas electron transfers and subsequent ionic annihilation appear to dominate at lower frequencies.

Methods

Material characterization

^1H and ^{13}C NMR spectra were obtained with JEOL ECS400. CDCl_3 was used as a deuterated solvent and all measurements were performed at ambient temperature. Chemical shifts were reported in δ (ppm), using tetramethylsilane as internal standards. Atmospheric pressure chemical ionization (APCI) mass spectra were measured with a timsTOF (Bruker).

Preparation of solutions

For PL samples, 80 mM TpAT-tFFO and 80 mM TpATtBu-tFFO were each weighed into separate vials. A mixture of anhydrous toluene and anhydrous acetonitrile in 2:1 by volume was pipetted into each vial. The solutions were heated at 60°C on a hot plate for 30 minutes. These 80 mM solutions were subsequently diluted to prepare concentrations down to 0.1 mM. For the hyperfluorescence PL sample, 10 mM TBRb was weighed into a vial, and then the 80 mM TpAT-tFFO solution was pipetted in. For ECL solutions, we first prepared a solution containing 10 mM TBRb and 100 mM supporting electrolyte (tetrabutylammonium hexafluorophosphate). Next, 80 mM TpAT-tFFO and 80 mM TpATtBu-tFFO were each weighed into separate vials. The TBRb solution was subsequently pipetted to each vial, followed by 30 minutes of heating at 60°C .

PL and absorption measurement

The solutions were argon bubbled for longer than 30 minutes to remove residual oxygen. 700 μL quartz cuvettes were used for the PL characterization. The PL spectra and transient PL of the solutions were measured using a fluorescence lifetime spectrometer (FluoTime 250, PicoQuant) paired with a picosecond diode laser ($\lambda=373$ nm). UV-vis absorption was measured with a UV-vis spectrometer (Cary 50, Varian). The HOMO energy levels of TpAT-tFFO and TpATtBu-tFFO were determined utilizing photoelectron yield spectroscopy (AC-3, Riken Keiki). The band gaps were determined from UV-Vis absorption in 0.1 mM toluene solution. The LUMO energy levels were calculated from the HOMO energy levels and the band gaps. The HOMO and LUMO levels of TBRb are taken from reference ³². The PLQY values were determined by using an absolute PLQY spectrometer (C9920-02, Hamamatsu Photonics).

Device fabrication

A pair of rectangular glass substrates coated with two strips of 2 mm-wide ITO were used to fabricate each ECLD. The substrates were cleaned using a detergent solution (2% Hellmanex III in Milli-Q water) followed by isopropyl alcohol. After drying, the ITO surface was treated with UV-ozone for 15 minutes. The substrate pair was bonded with NOA 68 resin (Norland Products), which was mixed with 30 μm -sized microbeads (Sigma-Aldrich), to have four 4 mm^2 -size cross sections of ITO, and cured with UV light while being pressed using a custom-made holder (Detailed information can be found in ref. ¹⁵). The edges of the bonded substrates remained open, maintaining a 30 μm gap, as the resin was applied only as droplets to the edges and corners. The bonded substrates were then transferred to a nitrogen-filled glove box, where 65 μL of the ECL solution was pipetted into the gap between the ITO substrates to fill the structure. The open edges were sealed with 3035BT resin (Threebond International) and cured with UV light, resulting in a production of glass-glass devices. For the glass-mirror device, after cleaning the substrate, a 120 nm-thick silver layer followed by a 50 nm-thick aluminum oxide layer was deposited onto the bare-glass side of the ITO substrates using vacuum evaporation and atomic layer deposition techniques, respectively. After coating, the substrates underwent the cleaning process again. The ITO surface was treated with UV-ozone for 3

minutes. A pair of silver-coated and uncoated ITO substrates was then used to fabricate each glass-mirror device following the steps described above.

Device characterization

The device was mounted on a sample holder positioned at the center of a 55 cm by 55 cm sized dark box. *JVL* was characterized by a step-wise increase in the amplitude of sinusoidal voltage signal generated by a function generator (33220A, Agilent Technologies). The actual V_{rms} and I_{rms} values were recorded by a power analyzer (GPM-8213, GW Instek) during the voltage sweep. A silicon photodiode (PDA100A2, Thorlabs) positioned 168 mm from the device measured the photocurrent in AC mode. Spectral data were collected using a fiber-coupled spectrometer (Ocean HDX, Ocean Insight). A Lambertian distribution was assumed in the calculation of Φ_{ECL} . Operational lifetime was analyzed using the same setup, with the photocurrent recorded every second during the extended operation. The voltage amplitude was controlled in potentiostatic mode, while the amplitude was finely adjusted to ensure the rms current remained within an error range of 1.0 μA in galvanostatic mode. Custom software automatized all measurements.

Absorption spectroelectrochemistry

Spectroelectrochemical analysis was performed using a custom-built inverted microscope setup (Nikon Eclipse Ti2) equipped with 20x extra-long working distance air objective. The sample was illuminated by a white LED source (pE-4000, CoolLED). A beam splitter and a digital camera (C13440 Orca-Flash 4.0, Hamamatsu) ensured precise alignment of the observation area within the active region of the device. The transmitted light spectrum was recorded using a spectrometer (Andor Shamrock 500i) with a 1-second acquisition time. First, the transmission of the white LED was measured with the device turned off (I_{off} in Fig. 4a), followed by a measurement with the device turned on (I_{on}). Lastly, the ECL intensity was measured with the white LED switched off (I_{ECL}).

Acknowledgements

This work was financially supported by the Alexander von Humboldt Foundation (Humboldt-Professorship to M.C.G.), JSPS KAKENHI grant numbers:JP20H05840 (Grant-in-Aid for Transformative Research Areas, "Dynamic Exciton") and JP23KJ1253, the JSPS Core-to-Core Program grant No: JPJSCCA20220004, the International Collaborative Research Program of Institute for Chemical Research, Kyoto University grant number:2024-126. A.P. acknowledges funding from the European Molecular Biology Organization through the EMBO Postdoctoral Fellowship (675-2022). The quantum chemical calculations were performed on the SuperComputer System, Institute for Chemical Research, Kyoto University.

Author contributions

C.-K.M., H.K., and M.C.G. conceived the project. C.-K.M. conducted PL measurements, manufactured ECLDs, and characterized them. Y.Y. and Y. K. conducted PL measurements for the tFFO-based molecules. S.F. synthesized TADF emitters. A.P. contributed to the spectroelectrochemical analysis. J.F.B. built the device characterization setup. C.-K.M., H.K., and M.C.G. mainly wrote the manuscript.

Competing interests

The authors declare no competing interests.

Data availability

All primary data for all figures and extended data figures are available from the corresponding author upon request.

References

- 1 Ma, C., Cao, Y., Gou, X. & Zhu, J.-J. Recent progress in electrochemiluminescence sensing and imaging. *Anal. Chem.* **92**, 431-454 (2019).
- 2 Muzyka, K. Current trends in the development of the electrochemiluminescent immunosensors. *Biosens. Biodelectron.* **54**, 393-407 (2014).
- 3 Miao, W. Electrogenenerated chemiluminescence and its biorelated applications. *Chem. Rev.* **108**, 2506-2553 (2008).
- 4 Hao, N. & Wang, K. Recent development of electrochemiluminescence sensors for food analysis. *Anal. Bioanal. Chem.* **408**, 7035-7048 (2016).
- 5 Shen, Y., Gao, X., Lu, H.-J., Nie, C. & Wang, J. Electrochemiluminescence-based innovative sensors for monitoring the residual levels of heavy metal ions in environment-related matrices. *Coord. Chem. Rev.* **476**, 214927 (2023).
- 6 Kasahara, T. *et al.* Recent advances in research and development of microfluidic organic light-emitting devices. *J. Photopolym. Sci. Tech.* **30**, 467-474 (2017).
- 7 Cho, K. G. *et al.* Light-Emitting Devices Based on Electrochemiluminescence Gels. *Adv. Funct. Mater.* **30** (2020).
- 8 Nobeshima, T., Morimoto, T., Nakamura, K. & Kobayashi, N. Advantage of an AC-driven electrochemiluminescent cell containing a Ru(bpy)₃²⁺ complex for quick response and high efficiency. *J. Mater. Chem.* **20** (2010).
- 9 Cao, Z., Shu, Y., Qin, H., Su, B. & Peng, X. Quantum dots with highly efficient, stable, and multicolor electrochemiluminescence. *ACS Cent. Sci.* **6**, 1129-1137 (2020).
- 10 Chu, K., Ding, Z. & Zysman-Colman, E. Materials for Electrochemiluminescence: TADF, Hydrogen-Bonding, and Aggregation- and Crystallization-Induced Emission Luminophores. *Chemistry* **29**, e202301504 (2023).
- 11 Okumura, R., Takamatsu, S., Iwase, E., Matsumoto, K. & Shimoyama, I. in *2009 IEEE 22nd International Conference on Micro Electro Mechanical Systems*. 947-950 (IEEE).
- 12 Kwon, D. K. & Myoung, J. M. Wearable and Semitransparent Pressure-Sensitive Light-Emitting Sensor Based on Electrochemiluminescence. *ACS Nano* **14**, 8716-8723 (2020).
- 13 Yee, H. *et al.* Extending the Operational Lifetime of Electrochemiluminescence Devices by Installing a Floating Bipolar Electrode. *Small* **20**, 2307190 (2024).
- 14 Laser, D. & Bard, A. J. Electrogenenerated Chemiluminescence: XXIII. On the Operation and Lifetime of ECL Devices. *J. Electrochem. Soc.* **122**, 632 (1975).
- 15 Moon, C. K., Butscher, J. F. & Gather, M. C. An Exciplex-Based Light-Emission Pathway for Solution-State Electrochemiluminescent Devices. *Adv. Mater.* **35**, 2302544 (2023).
- 16 Moon, C. K. & Gather, M. C. Absolute quantum efficiency measurements of electrochemiluminescent devices through electrical impedance spectroscopy. *Adv. Opt. Mater.* **12**, 2401253 (2024).
- 17 Uoyama, H., Goushi, K., Shizu, K., Nomura, H. & Adachi, C. Highly efficient organic light-emitting diodes from delayed fluorescence. *Nature* **492**, 234-238 (2012).
- 18 Kaji, H. *et al.* Purely organic electroluminescent material realizing 100% conversion from electricity to light. *Nat. Comm.* **6**, 8476 (2015).

- 19 Ishimatsu, R. *et al.* Electrogenenerated chemiluminescence of donor–acceptor molecules with thermally activated delayed fluorescence. *Angew. Chem. Int. Ed.* **53**, 6993-6996 (2014).
- 20 Huang, P. *et al.* Polymer electrochemiluminescence featuring thermally activated delayed fluorescence. *Chem. Phys. Chem.* **22**, 726-732 (2021).
- 21 Huang, P. *et al.* Studies on annihilation and coreactant electrochemiluminescence of thermally activated delayed fluorescent molecules in organic medium. *Molecules* **27**, 7457 (2022).
- 22 Ishimatsu, R. *et al.* Solvent effect on thermally activated delayed fluorescence by 1, 2, 3, 5-tetrakis (carbazol-9-yl)-4, 6-dicyanobenzene. *J. Phys. Chem. A* **117**, 5607-5612 (2013).
- 23 Legaspi, C. M. *et al.* Rigidity and polarity effects on the electronic properties of two deep blue delayed fluorescence emitters. *J. Phys. Chem. C* **122**, 11961-11972 (2018).
- 24 Nakanotani, H. *et al.* High-efficiency organic light-emitting diodes with fluorescent emitters. *Nat. Comm.* **5**, 4016 (2014).
- 25 Zhao, B. *et al.* Highly efficient red OLEDs using DCJTb as the dopant and delayed fluorescent exciplex as the host. *Sci. Rep.* **5**, 10697 (2015).
- 26 Kim, K.-H., Yoo, S.-J. & Kim, J.-J. Boosting triplet harvest by reducing nonradiative transition of exciplex toward fluorescent organic light-emitting diodes with 100% internal quantum efficiency. *Chem. Mater.* **28**, 1936-1941 (2016).
- 27 Wada, Y., Nakagawa, H., Matsumoto, S., Wakisaka, Y. & Kaji, H. Organic light emitters exhibiting very fast reverse intersystem crossing. *Nat. Photon.* **14**, 643-649 (2020).
- 28 Ko, E.-S. *et al.* Pulsed Driving Methods for Enhancing the Stability of Electrochemiluminescence Devices. *ACS Photon.* **5**, 3723-3730 (2018).
- 29 Tsuneyasu, S., Ichihara, K., Nakamura, K. & Kobayashi, N. Why were alternating-current-driven electrochemiluminescence properties from Ru(bpy)₃²⁺ dramatically improved by the addition of titanium dioxide nanoparticles? *Phys. Chem. Chem. Phys.* **18**, 16317-16324 (2016).
- 30 Kong, S. H., Lee, J. I., Kim, S. & Kang, M. S. Light-Emitting Devices Based on Electrochemiluminescence: Comparison to Traditional Light-Emitting Electrochemical Cells. *ACS Photon.* **5**, 267-277 (2017).
- 31 Yasuji, K., Sakanoue, T., Yonekawa, F. & Kanemoto, K. Visualizing electroluminescence process in light-emitting electrochemical cells. *Nat. Comm.* **14**, 992 (2023).
- 32 Liu, T.-H. *et al.* Highly efficient yellow and white organic electroluminescent devices doped with 2,8-di(t-butyl)-5,11-di[4-(t-butyl) phenyl]-6,12-diphenylnaphthacene. *Appl. Phys. Lett.* **85**, 4304-4306 (2004).

Electrochemically induced hyperfluorescence based on the formation of charge-transfer excimers

Chang-Ki Moon^{1,2}, Yuka Yasuda³, Yu Kusakabe³, Anna Popczyk¹, Shohei Fukushima³, Julain Butscher¹, Hironori Kaji^{3*}, Malte C. Gather^{1,2*}

¹Humboldt Centre for Nano- and Biophotonics, Institute of Light and Matter, Department of Chemistry, University of Cologne, Greinstr. 4-6, 50939 Köln, Germany

²Organic Semiconductor Centre, School of Physics and Astronomy, University of St Andrews, North Haugh, St Andrews KY16 9SS, United Kingdom

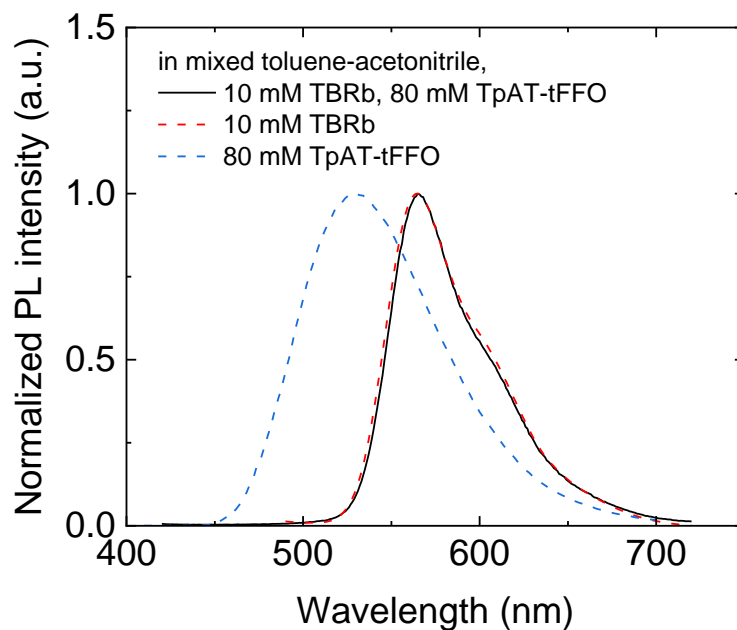
³Institute for Chemical Research, Kyoto University, Uji, Kyoto, Japan

Supplementary Table 1. TADF parameters of TpAT-tFFO in various concentrations in mixed toluene and acetonitrile solutions. The lifetime parameters are from for transient PL curves using equation, $I(t) = I_p \exp(-t/\tau_p) + I_d \exp(-t/\tau_d)$. The analyses for k_{ISC} and k_{RISC} used the method described in Methods section in reference ¹.

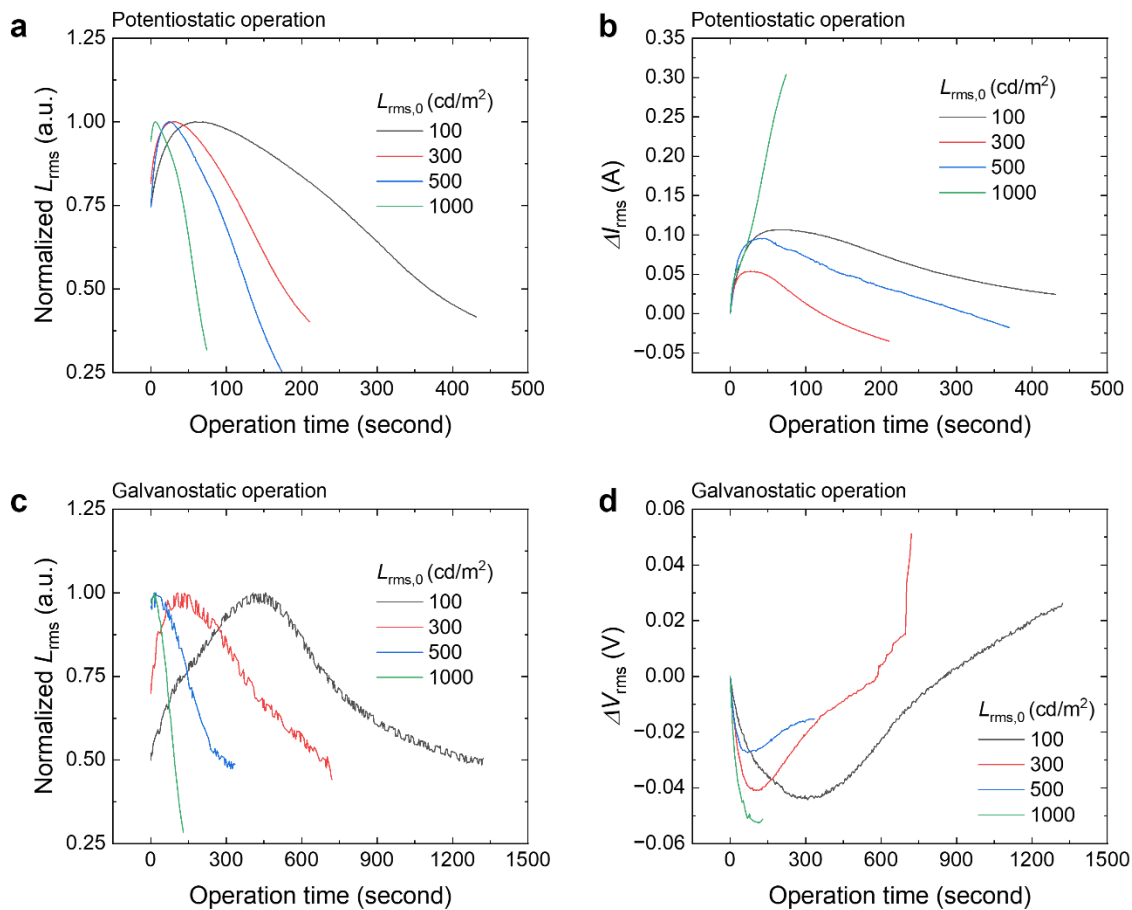
Concentration (mM)	State	I_p	τ_p (ns)	I_d	τ_d (ns)	Φ_d/Φ_p	Φ_{PL}	k_{ISC} ($10^7/s$)	k_{RISC} ($10^7/s$)	$k_{ISC}k_{RISC}$ ($10^{14}/s$)
0.1	Monomer	0.837	17.3	0.144	977	9.73	0.84	4.02	1.42	5.70
0.3	Monomer	0.883	18.3	0.128	1150	9.16	0.84	4.03	1.07	4.31
1	Mixed	0.837	20.2	0.158	928	8.65	-	-	-	-
3	Mixed	0.831	19.6	0.149	492	4.52	-	-	-	-
10	Mixed	0.838	20.4	0.158	355	3.27	-	-	-	-
30	Excimer	0.837	20.7	0.157	395	3.58	0.27	2.70	1.62	4.37
80	Excimer	0.794	18.6	0.131	1770	15.7	0.27	3.76	1.20	4.51

Supplementary Table 2. TADF parameters of TpATtBu-tFFO in various concentrations in mixed toluene and acetonitrile solutions. The lifetime parameters are from for transient PL curves using equation, $I(t) = I_p \exp(-t/\tau_p) + I_d \exp(-t/\tau_d)$. We found that TpATtBu-tFFO is a TADF molecule with high sensitivity to oxygen. Prior to PL measurement, each solution was purged with argon for 30 minutes to minimize oxygen interference. However, oxygen may infiltrate the solution and quench the triplet states of TpATtBu-tFFO during the measurement in the atmosphere. Due to this, potential errors in the ISC and RISC parameters of TpATtBu-tFFO cannot be ruled out.

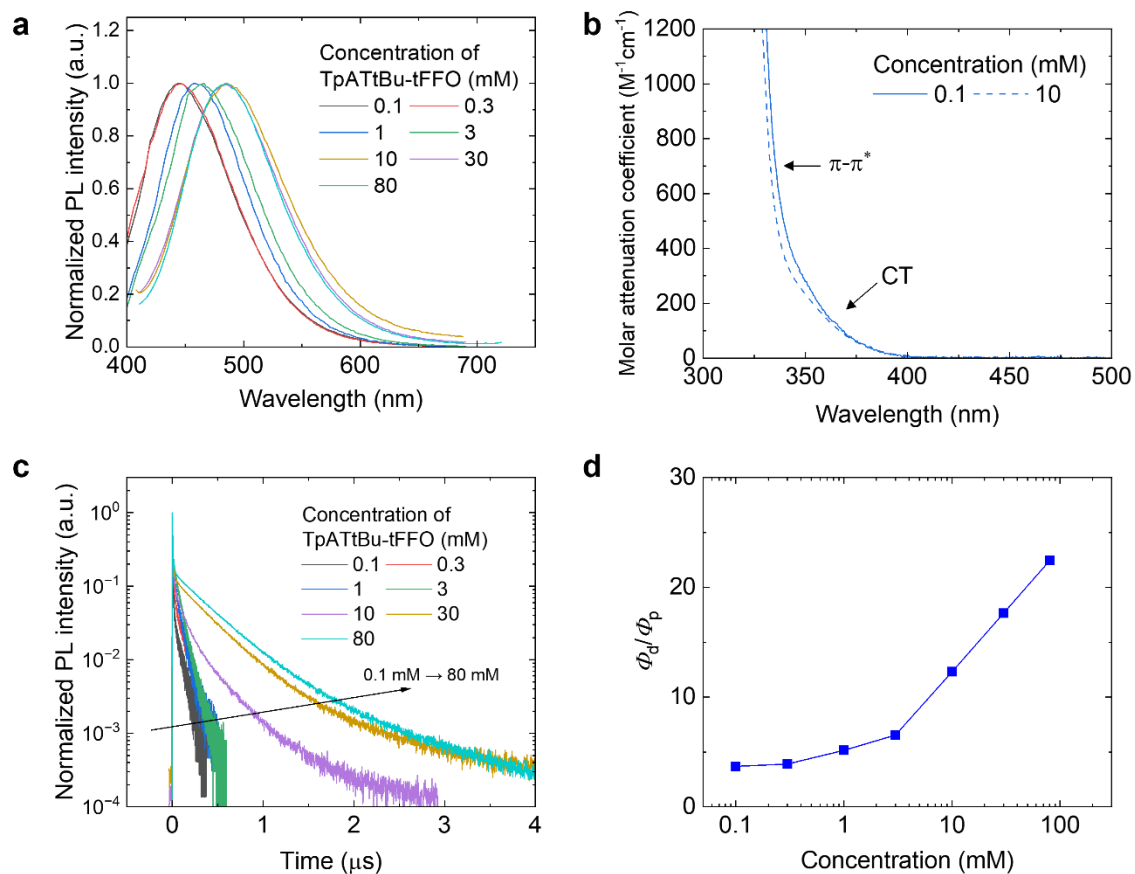
Concentration (mM)	State	I_p	τ_p (ns)	I_d	τ_d (ns)	Φ_d/Φ_p	Φ_{PL}	k_{ISC} ($10^7/s$)	k_{RISC} ($10^7/s$)	$k_{ISC}k_{RISC}$ ($10^{14}/s$)
0.1	Monomer	0.744	2.61	0.160	44.8	3.68	0.52	18.5	16.9	313
0.3	Monomer	0.737	2.95	0.144	53.5	3.90	0.52	16.7	14.8	247
1	Mixed	0.667	3.18	0.193	56.4	5.14	-	-	-	-
3	Mixed	0.725	3.44	0.254	64.2	6.53	-	-	-	-
10	Excimer	0.895	2.44	0.082	327	12.3	0.50	34.1	4.53	154
30	Excimer	0.835	3.06	0.138	328	17.6	0.50	24.3	7.21	175
80	Excimer	0.855	3.12	0.158	379	22.4	0.50	23.1	8.23	190



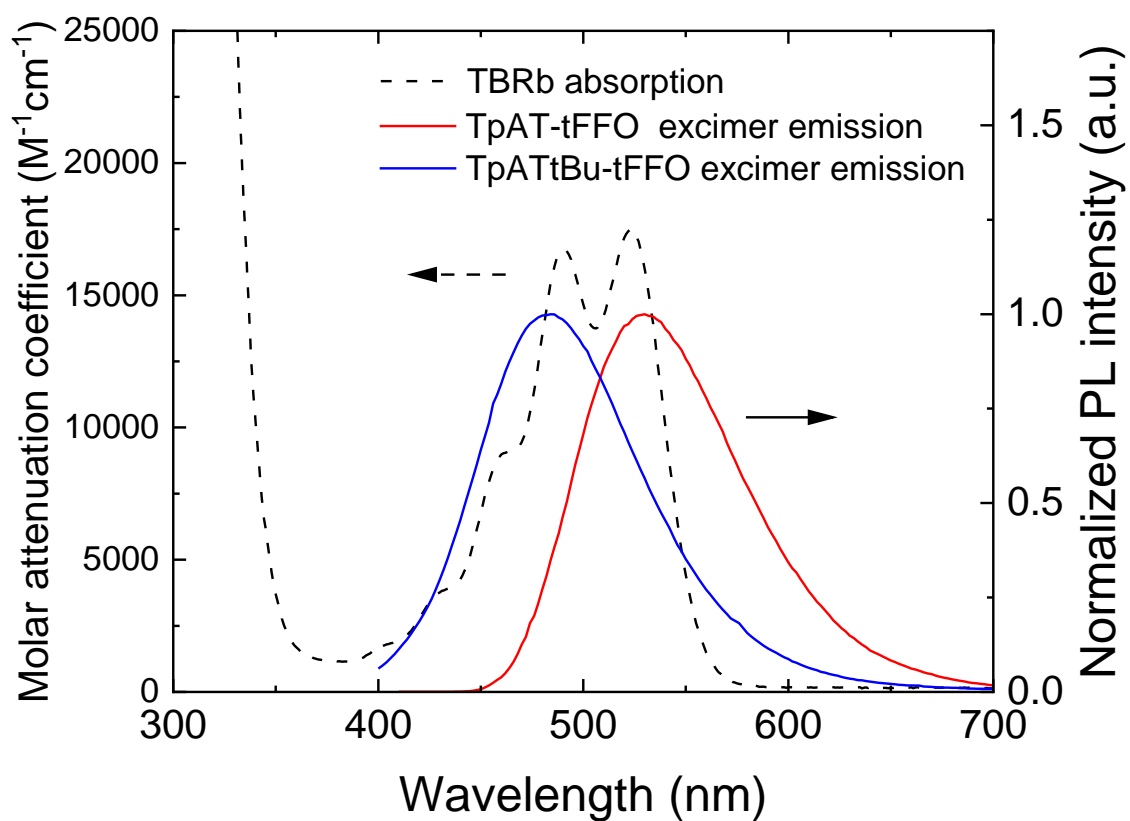
Supplementary Fig. 1. PL spectra of the mixed toluene-acetonitrile solution containing 10 mM TBRb and 80 mM TpAT-tFFO, both together and individually. Both TBRb and TpAT-tFFO molecules are excited by $\lambda = 373$ nm light. In the mixture of TBRb and TpAT-tFFO, the emission is solely from TBRb due to rapid energy transfer from TpAT-tFFO excimers to TBRb molecules,



Supplementary Fig. 2. Measurement of operational lifetime of the TpAT-tFFO device. **a**, Luminance over time under potentiostatic operation at various initial luminance values and **b**, consequent changes in the current. **c**, Luminance over time **e** under galvanostatic operations and **d**, changes in the applied voltage for maintaining current. Application of the voltage leads to re-distribution of molecules and ions within the liquid layer. That results in an initial increase in luminance along with increase in device current under the potentiostatic operation and decrease in the voltage under the galvanostatic operation. The LT50 value was estimated as the time when the brightness decreased by half of the maximum value at each operation.



Supplementary Fig. 3. Photoluminescence characteristics of TpATtBu-tFFO solutions. a, PL spectra, **b,** molar attenuation coefficient, **c,** transient PL, and **d,** the PLQY ratio of delayed fluorescence to prompt fluorescence of TpATtBu-tFFO by various concentrations in mixed toluene-acetonitrile solution 2:1 by volume.



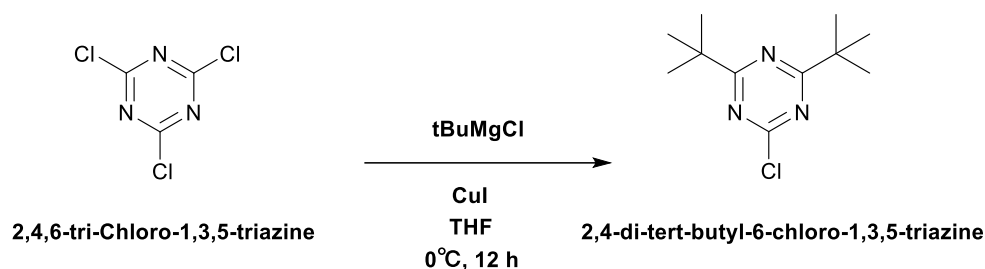
Supplementary Fig. 4. Absorption spectrum of TBRb, emission spectra of TpAT-tFFO and TpATtBu-tFFO excimers.

Synthesis of TpAT-tFFO

TpAT-tFFO was prepared according to reference¹.

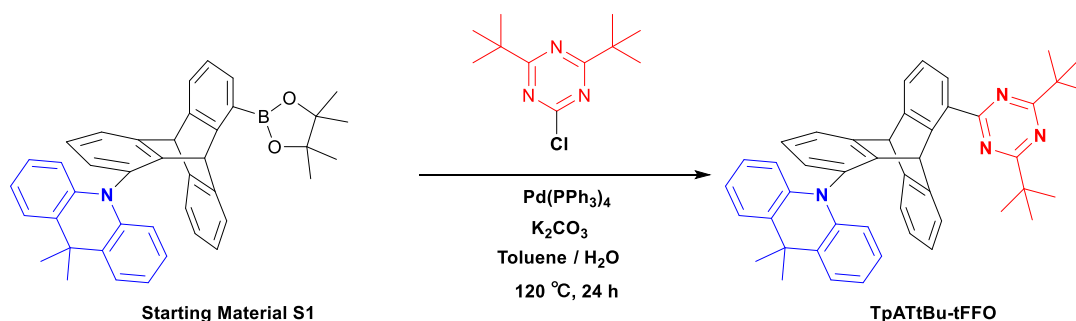
Synthesis of TpATtBu-tFFO

The synthesis scheme of TpATtBu-tFFO is summarized in Supplementary Scheme 1 and 2. The starting material S1 was prepared according to reference¹.



Supplementary Scheme 1. Synthesis of 2,4-di-tert-butyl-6-chloro-1,3,5-triazine.

In a 100-mL two neck round bottom flask, 2,4,6-tri-chloro-1,3,5-triazine (2.08 g, 11.3 mmol) and copper(I) iodide (70.5 mg, 0.37 mmol) were dissolved in 12 mL of dehydrated THF under an Ar atmosphere and the solution was cooled to -10°C . After 2 h stirring, 13.6 mL (27.1 mmol) of tert-butylmagnesium chloride solution 2.0 M in THF was slowly dropwised to the stirred solution. After stirring at 0°C for 2 h and at r.t. for 12 h, the reaction mixture was quenched with 50 ml of 2.4 M HCl aqueous solution. The resulting mixture layer was extracted with 50 mL of ethyl acetate three times. The crude mixture was concentrated under reduced pressure and then purified by silica gel column chromatography using hexane/dichloromethane = 9/1 as eluent. 2.32 g (10.2 mmol) of 2,4-di-tert-butyl-6-chloro-1,3,5-triazine (Supplementary Scheme 1) was obtained in 90% yield.



Supplementary Scheme 2. Synthesis of TpATtBu-tFFO.

A 45-mL portion of deoxidized toluene and 4.5 mL of 2 M aqueous potassium carbonate (12.0 mmol) were added to a 100-mL round bottom Schlenk flask containing Starting Material S1

(0.42 g, 0.75 mmol), 2,4-di-tert-butyl-6-chloro-1,3,5-triazine (0.29 g, 1.27 mmol), and Pd(PPh₃)₄ (84 mg, 0.075 mmol). After three freeze-pump-thaw cycles under an Ar atmosphere, the mixture was stirred at 120 °C for 24 h. After the reaction mixture was cooled to ambient temperature, 40 mL of distilled water was added, and the organic layer was extracted with 50 mL of ethyl acetate three times. The combined organics were dried over sodium sulfate, concentrated under reduced pressure and then purified by column chromatography using hexane/dichloromethane = 4/1. 0.366 g (0.56 mmol) of TpATtBu-tFFO was obtained in 74% yield.

¹H NMR (400 MHz, CDCl₃, δ): 8.11 (dd, J = 8.0, 1.1 Hz, 1H), 7.62-7.60 (m, 1H), 7.53 (d, J = 7.2 Hz, 1H), 7.49 (d, J = 7.0 Hz, 1H), 7.43 (dd, J = 7.8, 1.4 Hz, 1H), 7.32 (d, J = 6.4 Hz, 1H), 7.23-7.15 (m, 3H), 7.13 (s, 1H), 7.10-7.06 (m, 1H), 7.03 (td, J = 7.3, 1.3 Hz, 1H), 6.98-6.94 (m, 1H), 6.86-6.81 (m, 2H), 6.55-6.51 (m, 1H), 6.38-6.34 (m, 1H), 5.84 (dd, J = 8.1, 1.0 Hz, 1H), 5.72 (dd, J = 8.1, 1.0 Hz, 1H), 5.66 (s, 1H), 1.89 (s, 3H), 1.26 (s, 3H), 1.17 (s, 18H). ¹³C NMR (101 MHz, CDCl₃, δ): 184.1, 171.3, 148.1, 147.2, 146.4, 145.8, 144.6, 143.8, 140.9, 140.5, 136.1, 133.4, 130.6, 129.9, 128.5, 128.0, 126.7, 126.5, 126.2, 126.1, 125.7, 125.2, 125.2, 123.7, 123.5, 123.4, 123.4, 120.8, 120.3, 114.8, 113.3, 77.3, 77.0, 76.7, 54.8, 45.6, 39.2, 36.1, 33.0, 28.8, 23.6.

APCI-MS (m/z): [M+H]⁺ calcd. for C₄₆H₄₅N₄, XXXX; found, XXXX.

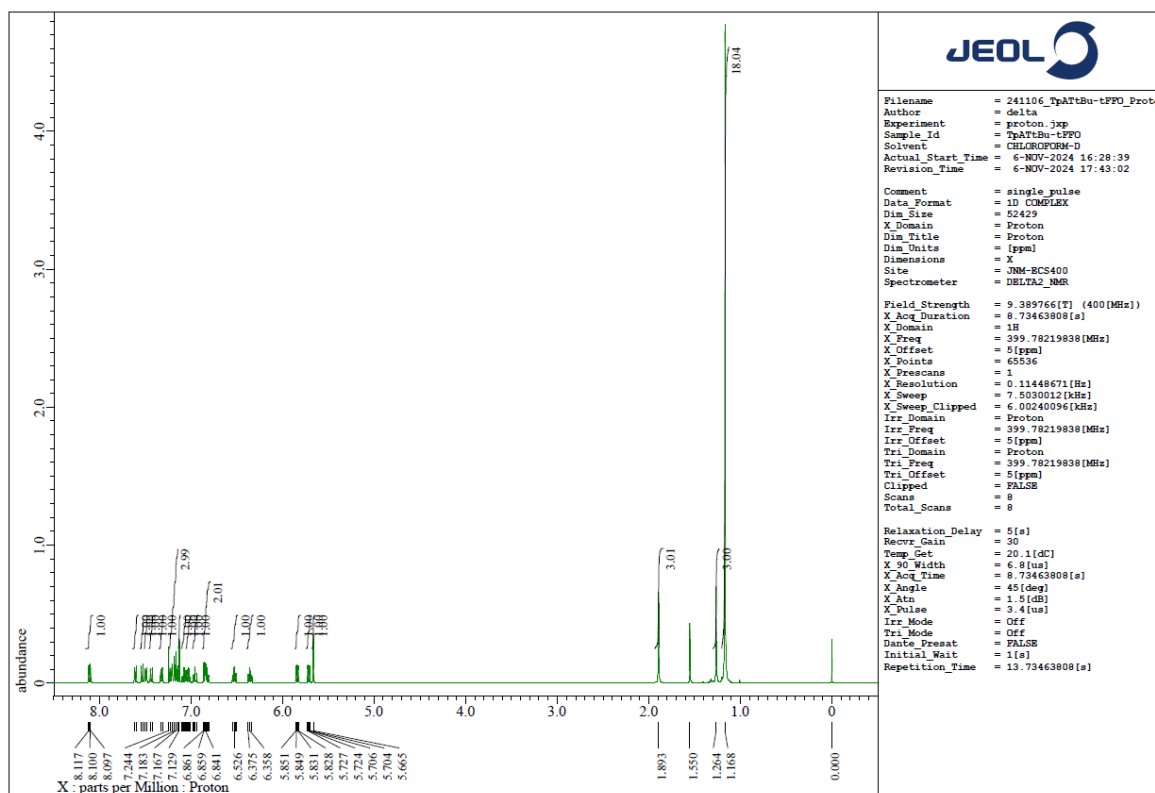


Figure S5. ^1H NMR spectrum of TpATtBu-tFFO.

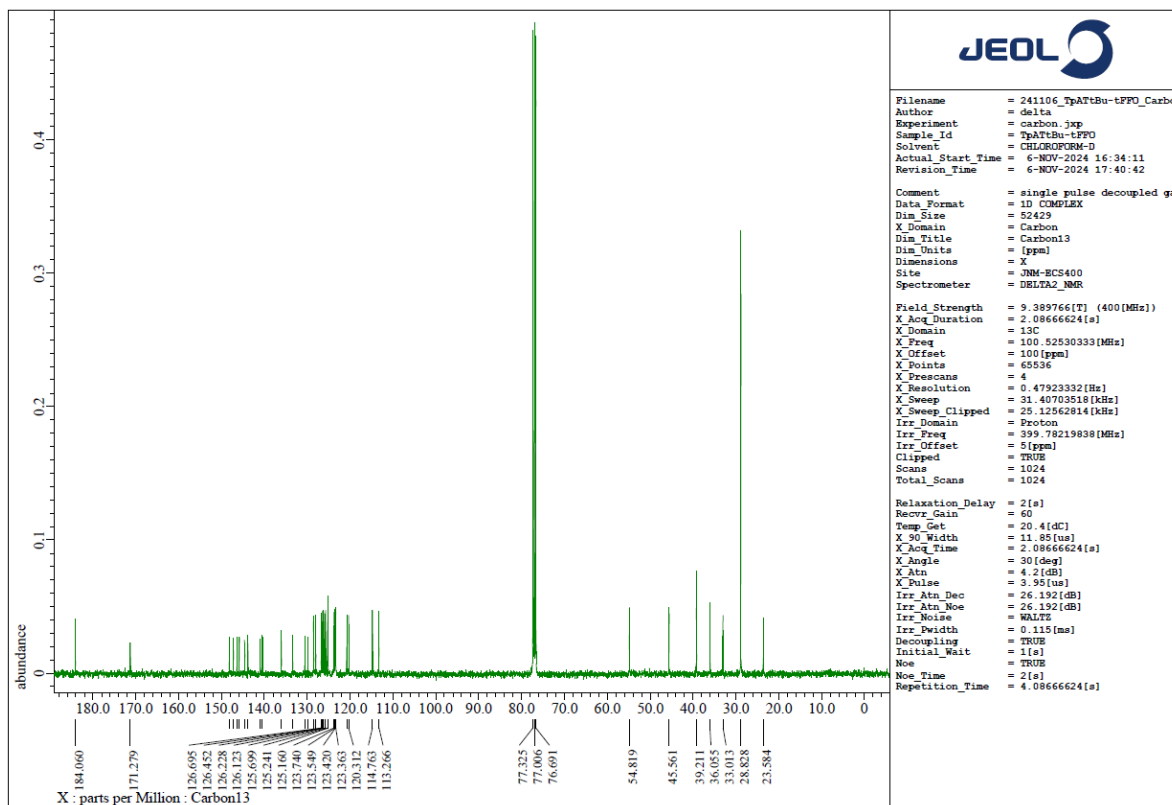


Figure S6. $^{13}\text{C}\{^1\text{H}\}$ NMR spectrum of TpATtBu-tFFO.

References

1. Y. Wada, H. Nakagawa, S. Matsumoto, Y. Wakisaka and H. Kaji, *Nat. Photon.*, 2020, **14**, 643-649.